International Journal of Heat and Fluid Flow 29 (2008) 602–611

Contents lists available at ScienceDirect

International Journal of Heat and Fluid Flow

journal homepage: www.elsevier.com/locate/ijhff

Turbulent structures and statistics in turbulent channel flow with two-dimensional slits

Soichiro Makino *, Kaoru Iwamoto [1], Hiroshi Kawamura

Department of Mechanical Engineering, Tokyo University of Science, Noda-shi, Chiba 278-8510, Japan

ARTICLE INFO

Article history:
Received 7 November 2007
Received in revised form 5 March 2008
Accepted 8 March 2008
Available online 7 May 2008

Keywords:
Direct numerical simulation
Turbulence
Separation and reattachment
Turbulent structure
Two-dimensional obstacle
Slit

ABSTRACT

Direct numerical simulation (DNS, hereafter) of turbulent channel flow with periodic two-dimensional slits has been performed in order to investigate the turbulent statistics and the turbulent structures behind the slits. The Reynolds numbers based on the friction velocity and the channel half width are 10–1500. In the wake region, the mean flow becomes asymmetric with respect to the centerline of the geometry through the Coanda effect. Large-scale vortices are generated at the height of the slit edges. These vortices become deformed in various scenarios and break up into disordered small-scale structures in the shear layers behind the slit. The small-scale vortices are convected toward the channel center. The budgets of the Reynolds stresses have been computed. The significant differences are found between the budgets in this study and those in a backward-facing step turbulence. The positive Reynolds shear stress $\overline{u'v'}$ is observed owing to the flow contraction just behind the slit. The wake region was classified into several categories based upon the budgets of the Reynolds stresses and turbulent structures.

1. Introduction

Separation and reattachment of turbulent flows occur in many practical engineering applications. In the numerical studies of separated flows, the flow over a backward-facing step (e.g., Friedrich and Arnal, 1990; Le et al., 1997; Avancha and Pletcher, 2002), the ribbed channel (e.g., Leonardi et al., 2003; Sewall et al., 2006) and the roughened channel flow (e.g., Nagano et al., 2004; Krogstad et al., 2005) are frequently employed. In particular, the flow through a two-dimensional backward-facing step is the most popular. Le et al. (1997) performed DNS of a turbulent flow over a backward-facing step and evaluated several quantities such as the reattachment length, the Reynolds stresses and the turbulent kinetic energy budgets. The effect of step height was studied by Chen et al. (2006). The Kelvin–Helmholtz (K–H) vortices and the longitudinal vortices were observed behind the step (Neto et al., 1993). Recently, the simulations for more practical configurations have been performed, for example, the flow over riblets (Stalio and Nobile, 2003) or with one wavy wall (Choi and Suzuki, 2005).

On the other hand, DNS of a turbulent flow with slits has never been performed to the authors' knowledge. The slits are often used to control the flow rate and to enhance the mixing in practical mechanical equipments. In this flow, the separation, the reattachment and also the contraction occur near and behind the slit. Therefore, the study of flow field with slits is useful to investigate the effects of the flow acceleration/contraction in the separated flow. In this study, the flow acceleration is defined as the positive streamwise mean velocity gradient ($\partial U/\partial x > 0$) and the flow contraction $\partial V/\partial x \neq 0$ and/or $\partial V/\partial y \neq 0$, where U is the streamwise mean velocity and V the wall-normal mean velocity.

In the present work, DNS of a laminar and a turbulent channel flow with periodic two-dimensional slits has been carried out for $Re_{\tau 0} = u_{\tau 0}\delta/\nu = 10$–$1500$, where $u_{\tau 0}$ is the friction velocity defined later, δ the channel half width and ν the kinematic viscosity. The purposes of this study are to obtain the turbulent statistics for the development in turbulence modeling and to examine the relationship between the turbulent structures and turbulent statistics behind the slit.

2. Numerical procedures

The configuration of the computational domain is shown in Fig. 1a. A periodically repeating spatial unit with one two-dimensional slit is simulated. The periodic boundary conditions are employed in the streamwise (x) and spanwise (z) directions. The no-slip boundary conditions are used on all the walls. The direct forcing immersed boundary method (Fadlum et al., 2000) is applied on the plates in each side of the slit. The regular grid is applied in the streamwise direction to use the FFT (Fast Fourier Transform) in the solution of pressure-Poisson's equation. To ensure the grid resolution even close to the slit wall, a large mesh

* Corresponding author.
E-mail address: a7502126@rs.noda.tus.ac.jp (S. Makino).
[1] Present address: Department of Mechanical Systems Engineering, Tokyo University of Agriculture and Technology, Koganei-shi, Tokyo 184-8588, Japan.

0142-727X/$ - see front matter © 2008 Elsevier Inc. All rights reserved.
doi:10.1016/j.ijheatfluidflow.2008.03.010

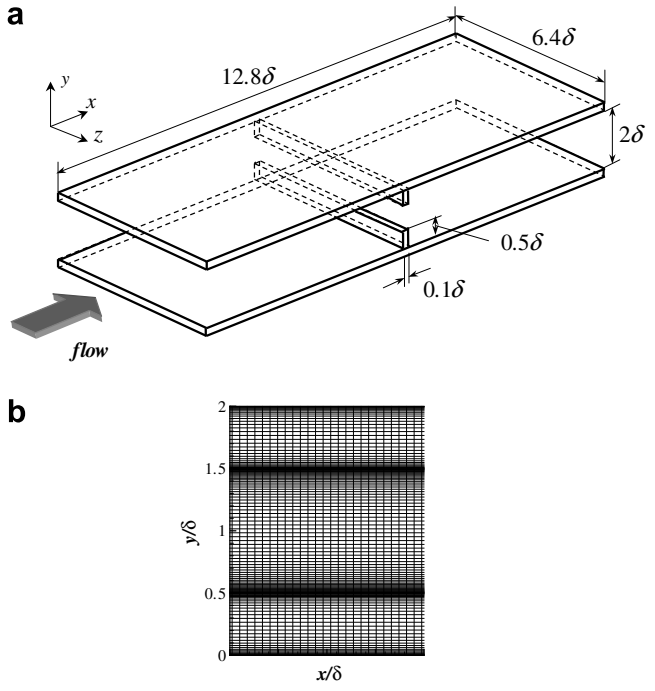

Fig. 1. (a) Configuration of the computational domain; (b) computational mesh.

number is employed in the streamwise direction (see Table 1). In the wall-normal direction, the density of the computational mesh is high at the height of the slit edges and near the walls (see Fig. 1b).

The governing equations are the incompressible continuity and Navier–Stokes equations:

$$\frac{\partial u_i^*}{\partial x_i^*} = 0, \tag{1}$$

$$\frac{\partial u_i^*}{\partial t^*} + \frac{\partial (u_i^* u_j^*)}{\partial x_j^*} = -\frac{\partial p^*}{\partial x_i^*} + \frac{1}{Re_{\tau 0}} \frac{\partial^2 u_i^*}{\partial x_j^* \partial x_j^*} - \frac{\partial \overline{p^*}}{\partial x_i^*} \delta_{i1} + F_i^*, \tag{2}$$

where u and p denote velocity vector and pressure, respectively. The quantities with superscript * indicate that they are normalized by $u_{\tau 0}$ and δ. The term $-\partial \overline{p^*}/\partial x_i^* \cdot \delta_{i1}$ is the non-dimensionalized mean streamwise pressure gradient, which drives the mean flow. The friction velocity $u_{\tau 0}$ is defined as the one calculated from the given mean pressure gradient $-\partial \overline{p}/\partial x$ in the case of the plane channel without the slits, i.e.,

$$u_{\tau 0} = \sqrt{\frac{\tau_{w0}}{\rho}} = \sqrt{\frac{|-\partial \overline{p}/\partial x| \cdot \delta}{\rho}}, \tag{3}$$

where τ_{w0} is the wall shear stress in the case of the plane channel flow. The additional F_i^* in Eq. (2) is the body force term for the immersed boundary method.

The SMAC (simplified marker and cell) method is adopted for the coupling between the continuity and the Navier–Stokes equations. The second-order Crank–Nicolson scheme and the compact-storage third-order Runge–Kutta scheme are employed as the time-advance algorithm: the former for the vertical viscous term, the later for the other viscous and the convection terms. The velocity predictors are calculated by solving TDMA (tri-diagonal matrix algorithm) in the wall-normal direction. The pressure-Poisson's equation is solved with the FFT for the streamwise and spanwise directions and with the TDMA for the wall-normal one. The finite difference method is used for the spatial discretization: the second-order central scheme is employed in all the directions.

The computational conditions are summarized in Table 1. The ratio of slit height to channel height β is set to be 0.5, i.e., the

Table 1
Computational conditions

$Re_{\tau 0}(=u_{\tau 0} \cdot \delta/\nu)$	10	12.5	17.5	20	30	50	75	100	200	300	400	500	600	1500
$Re_b(=u_b \cdot 2\delta/\nu)$	40	55	90	110	180	295	425	565	1080	1600	2100	2625	3130	7800
β	0.5													
Domain $(L_x \times L_y \times L_z)$	$12.8\delta \times 2\delta \times 6.4\delta$													
Grid number	$128 \times 96 \times 64$							$512 \times 128 \times 256$						$1024 \times 256 \times 512$
$\langle u_\tau^* \rangle_{ave} = \langle u_\tau \rangle_{ave}/u_{\tau 0}$	0.73	0.68	0.57	0.55	0.54	0.53	0.52	0.48	0.40	0.38	0.33	0.29	0.26	0.24
$\Delta x/\langle \nu/\langle u_\tau \rangle_{ave}$	0.730	0.850	0.999	1.10	0.405	0.663	0.975	1.20	2.00	2.85	3.30	3.63	3.84	4.80
$\Delta y_{min}/\langle \nu/\langle u_\tau \rangle_{ave}$	0.014	0.016	0.019	0.021	0.024	0.040	0.059	0.072	0.121	0.172	0.199	0.218	0.235	0.260
$\Delta y_{max}/\langle \nu/\langle u_\tau \rangle_{ave}$	0.596	0.694	0.814	0.898	0.55	0.90	1.32	1.63	2.71	3.87	4.48	4.92	5.29	6.25
$\Delta z/\langle \nu/\langle u_\tau \rangle_{ave}$	0.730	0.850	0.999	1.10	0.405	0.663	0.975	1.20	2.00	2.85	3.30	3.63	3.84	4.80
Sampling time period $(T\ u_b/L_x)$	12–15													

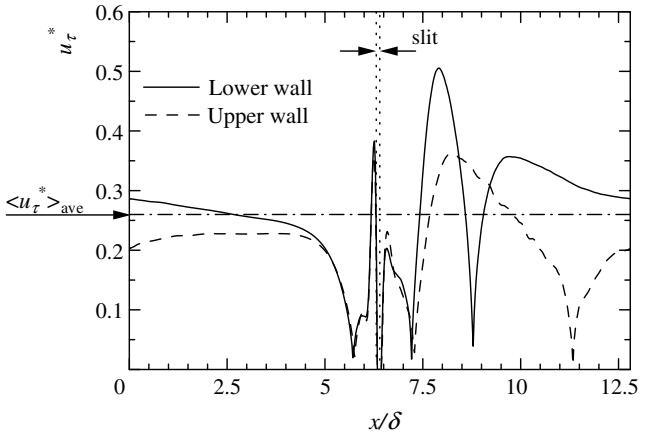

Fig. 2. The non-dimensionalized actual friction velocity profiles for $Re_{\tau 0} = 600$.

distance between the wall and slit edge h is 0.5δ in this study. The non-dimensionalized local friction velocity $u_\tau^* (= u_\tau/u_{\tau 0})$ for $Re_{\tau 0} = 600$ is shown in Fig. 2. The streamwise-averaged friction velocity $\langle u_\tau \rangle_{ave}/u_{\tau 0}$ is 0.26 in this case. The spatial resolutions are calculated from the streamwise-averaged friction velocity $\langle u_\tau \rangle_{ave}$ and seen in Table 1. In the DNS of a backward-facing step turbulence, the spatial resolutions are $\Delta x^* \simeq 10$ and $\Delta z^* \simeq 15$, based on the inlet boundary layer shear velocity (Le et al., 1997). In the present calculation, they are 4.8 or less. Therefore, the resolutions in this study are fine enough to obtain the second-order turbulence statistics.

3. Results and discussion

3.1. Asymmetry phenomena and mean reattachment length

The streamlines of the mean flow for $Re_{\tau 0} = 20$, 50, 300, 600, and 1500 are given in Fig. 3. The mean flow is asymmetry behind the slit in the cases of higher Reynolds numbers, which is similar to the flow in a sudden expansion (e.g., Cherdron et al., 1978; Fearn et al., 1990; Durst et al., 1993; Alleborn et al., 1997). These phenomena are referred to as the Coanda effect. The asymmetric direction depends on the initial flow field. We obtained the flow attachment to the upper and lower walls nearly with the same probability. In this study, the mean symmetric flow can be observed in the cases of $Re_\tau \leqslant 20$, i.e., $Re_b \leqslant 110$, and the mean flow becomes asymmetric in the cases of $Re_{\tau 0} \geqslant 30$ up to $Re_{\tau 0} = 1500$, i.e., $Re_b = 7800$.

In addition, we tested also an inlet–outlet boundary condition case (non-periodic) with a driver section which is a computational sub part to generate a fully developed turbulent channel flow for the inlet boundary condition (Inagaki et al., 2005). The convective boundary condition is applied at the outlet boundary of the main part. The domain size is $12.8\delta \times 2\delta \times 6.4\delta$ and the grid number $256 \times 128 \times 256$ for the driver section. For the main section, the domain is $16\delta \times 2\delta \times 6.4\delta$ and the grid is the $512 \times 128 \times 256$. The slit is stationed at 4δ in the streamwise direction from the connecting plane between the sub and main parts. The time-averaged streamlines in the case of the inlet–outlet boundary condition are shown in Fig. 4. The mean flow becomes asymmetric as seen in the of the periodic boundary condition. Therefore, the streamwise periodicity adds less effect on the asymmetry phenomena.

A large primary bubble is observed from the back-end of the slit to 9δ in the x-direction at the lower wall (L_{r1} in Fig. 3). In addition, a secondary bubble (B in Fig. 3) generates to approximately 7.3δ in the x-direction (see L_{r2} in Fig. 3), i.e., $1.8h$ from the slit for $Re_{\tau 0} = 600$. Le et al. (1997) reported that the length of the secondary bubble in the x-direction L_{r2} is $1.76h$ for a backward-facing step flow. Therefore, the length of the secondary bubble is almost same in both the cases.

The reattachment length L_{r1} and the secondary bubble length L_{r2} are shown in Fig. 5 as a function of the bulk Reynolds number. In this study, the reattachment location is determined by the location of $\partial U/\partial y = 0$ at the wall. The length L_{r1} is defined as the distance from the back-end of the slit to the reattachment location. Because the mean flow is asymmetric, the L_{r1} and the L_{r2} are obtained as an average of those on the upper and lower computational domain, i.e., the averaged reattachment point is the location of $1/2(\partial U/\partial y|_{lower} + \partial U/\partial y|_{upper}) = 0$. In the range of $Re_b < 400$, the L_{r1} increases with increasing the Reynolds number. On the other hand, in $Re_b > 400$ range, the reattachment length L_{r1} is characterized first by a sharp decrease and subsequently by a gradual one. These results are similar to those described in the case of the backward-facing step experiment (Armaly et al., 1983). One can clearly identify the laminar ($Re_b < 400$), the transitional and the turbulent ($400 < Re_b < 7800$) ranges as implied by the shape of this profile.

The secondary bubble cannot be observed in the laminar region ($Re_b < 400$). In the range of $400 < Re_b < 550$, the secondary bubble length L_{r2} increases with increasing the Reynolds number and it becomes almost constant in $Re_b > 550$ range. Therefore, the secondary bubble is generated in the transitional and the turbulent regime. In addition, the reattachment length L_{r1} at a higher Reynolds number ($Re_b > 2000$) is approximately $6h (= 3\delta)$ in this study. This corresponds roughly to the well-known length of $5 - 8h$ in the case of the turbulent flow over a backward-facing step (Lesieur, 1997).

3.2. Instantaneous vortex structures behind the slit

The vortex structures for $Re_{\tau 0} = 30$, 100, and 600 are shown in Fig. 6. The vortices are identified by the iso-surface of the second invariant of the velocity-gradient tensor defined as

$$II^* = -\frac{\partial u_i^*}{\partial x_j^*}\frac{\partial u_j^*}{\partial x_i^*} \tag{4}$$

The spanwise primary K–H vortices are visible in the shear layers behind the slit (A in Fig. 6(a-1)(b-1)(c-2)). These K–H vortices develop in different ways for the different Reynolds numbers.

In the case of $Re_{\tau 0} = 30$, they are distorted in the z-direction and longitudinal vortices are observed between them (B in Fig. 6 (a-1)(a-2)). A schematic view of these vortices is shown in Fig. 6d. The longitudinal vortices connect one spanwise K–H vortex with another one (C in Fig. 6(a-2)). This three-dimensional vortex structure resembles helical-pairing structure in a mixing layer (Comte et al., 1992) or in a backward-facing step flow (Neto et al., 1993).

For $Re_{\tau 0} = 100$, the K–H vortices become deformed more significantly in the y- and z-direction and break up into disordered small-scale structures. Fig. 6(b-2) shows the complex three-dimensional vortex structure with a lattice pattern. The similar vortex pattern is observed in a temporal mixing layer (Comte et al., 1992).

In the case of $Re_{\tau 0} = 600$, the smaller structures are shown in Fig. 6(c-1) and (c-2). The spanwise distorted K–H vortices are observed. The pairing or the lattice structure discussed above, however, is not clearly found because the three-dimensional perturbation increases more significantly.

3.3. Fundamental turbulent statistics

The streamwise mean velocity and the Reynolds stresses profiles in both the upstream and downstream sides of the silt are shown in Fig. 7, where x_r is the streamwise distance from the back-end of the slit. The positive value of x_r indicates the

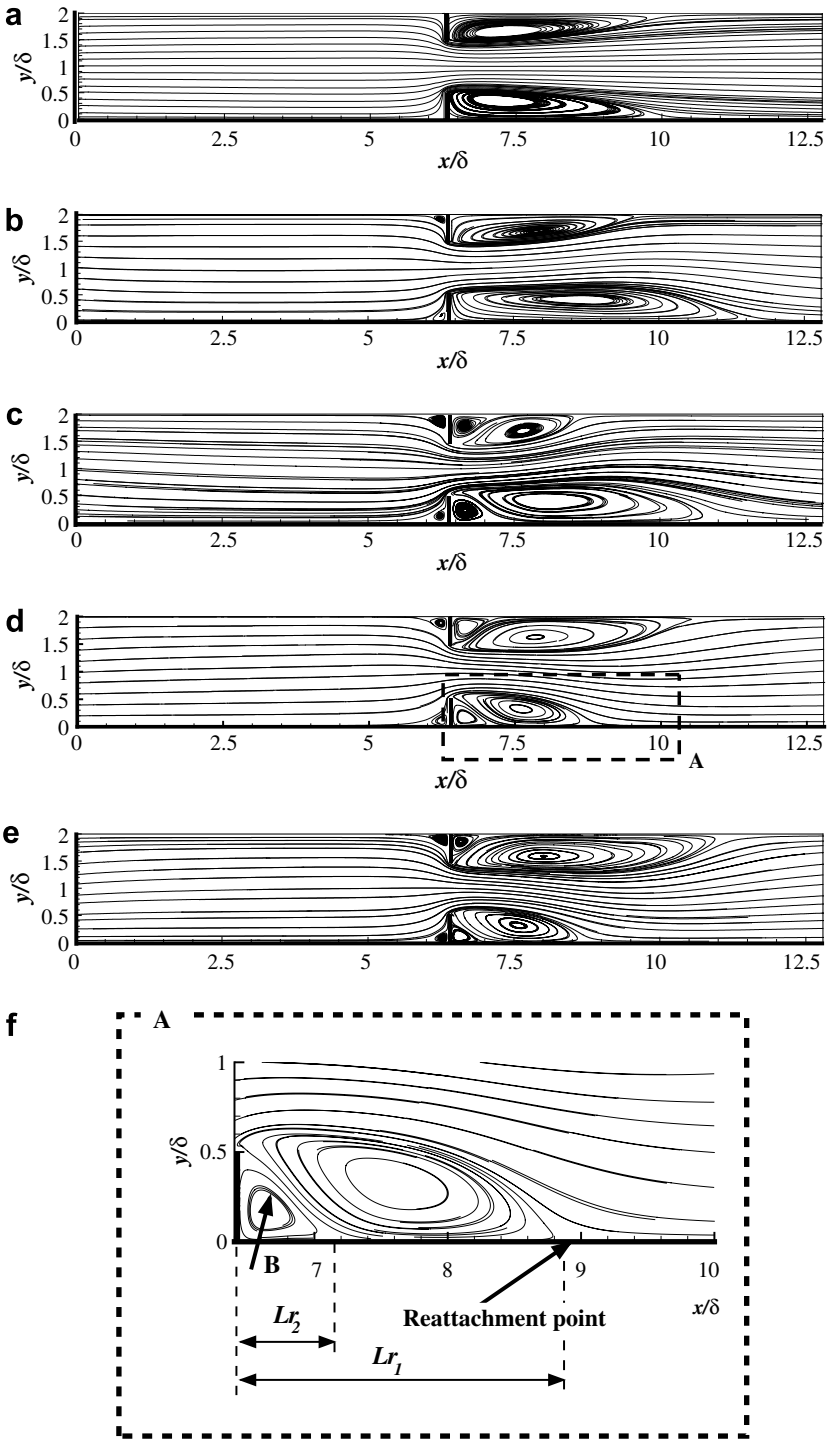

Fig. 3. Averaged streamlines. (a) $Re_{\tau 0} = 20$; (b) $Re_{\tau 0} = 50$; (c) $Re_{\tau 0} = 300$; (d) $Re_{\tau 0} = 600$; (e) $Re_{\tau 0} = 1500$; (f) enlarged view of the rectangular region A in (d).

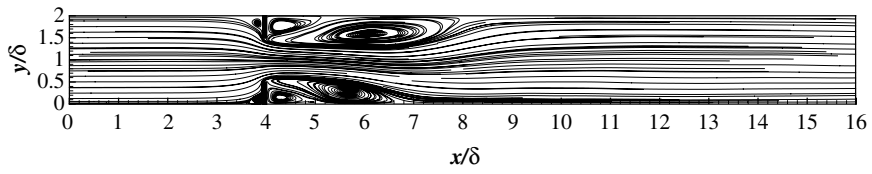

Fig. 4. Averaged streamlines in the case of the inlet–outlet boundary condition (non-periodic case).

downstream side and the negative, the upstream one. The fluctuation velocity u', v' and w' are in the streamwise, the wall-normal and the spanwise directions, respectively. In the upstream region ($x_r = -4, -3$ and -2), the mean velocity profiles are almost same

and the slight asymmetry can be observed. Very close to the slit ($x_r/\delta = -1$), the value of the mean velocity on the channel center, i.e., $y/\delta = 1$, becomes larger than those for $x_r/\delta = -4, -3, -2$ owing to the flow acceleration. At $x_r = 0$, the mean velocity becomes negative on top of the slit edges ($0.5 < y/\delta < 0.55$ and $1.45 < y/\delta < 1.5$) because small recirculation regions are generated (cf. the height of the slit edges are $y/\delta = 0.5$ and 1.5). The velocity attains its local maximum at $y/\delta \simeq 0.6$ or 1.4, not at near the centerline. This is because of the flow acceleration/contraction through the slit. The profiles become asymmetric significantly downstream of the slit. As for the Reynolds stresses upstream of the slit, they are larger than those in the channel center region as compared with those in plane channel flow (Kawamura et al., 1999). The sharp peaks can be seen in the $\overline{u'u'}$ and $\overline{v'v'}$ profiles at $x_r/\delta = 0$. These peak regions correspond to the shear layers. The $\overline{w'w'}$ exhibits four peaks, which can be observed in the same region of the channel with rods (Ashrafian et al., 2004). On the Reynolds shear stress $\overline{u'v'}$ at $x_r/\delta = 0$, it becomes positive (on the lower side of the channel) in the shear layer. The details of this issue will be discussed in the next section.

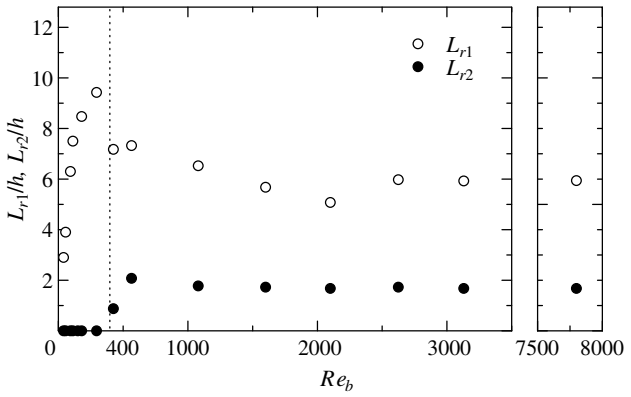

Fig. 5. Reynolds number dependence of reattachment length L_{r1}/h and secondary bubble length L_{r2}/h from the back-end of the orifice.

3.4. Classification of wake region based upon the turbulent structures and statistics

In this section, the relationship between the turbulent structures and the turbulent statistics in the case of $Re_{\tau 0} = 600$ are reported. In Fig. 8, the wake region is classified based upon the budgets of the Reynolds stresses and the turbulent structures in this study. The transport equation of the Reynolds stresses nondimensionalized by $u_{\tau 0}^4/\nu$ is expressed as

$$\frac{\partial}{\partial t}\overline{u_i'^* u_j'^*} = P_{ij} + T_{ij} + D_{ij} + \Pi_{ij} + \phi_{ij} + \epsilon_{ij} + C_{ij}, \tag{5}$$

Production term:

$$P_{ij} = -\overline{u_j'^* u_k'^*}\frac{\partial U_i^*}{\partial x_k^+} - \overline{u_i'^* u_k'^*}\frac{\partial U_j^*}{\partial x_k^+}, \tag{6}$$

Turbulent diffusion term:

$$T_{ij} = -\frac{\partial}{\partial x_k^+}\overline{u_i'^* u_j'^* u_k'^*}, \tag{7}$$

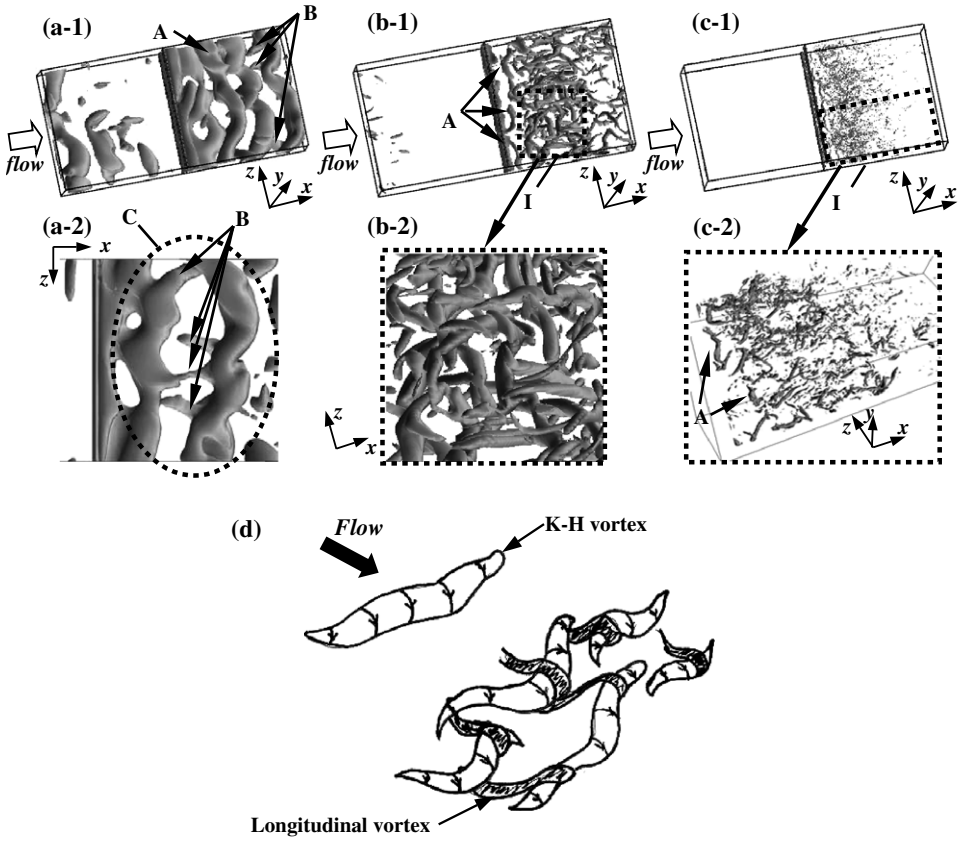

Fig. 6. Iso-surfaces of the second invariant of the velocity-gradient tensor II^*. (a-1) $II^* \leqslant -90$ for $Re_{\tau 0} = 30$; (a-2) bottom view of the wake region in (a-1); (b-1) $II^* \leqslant -250$ for $Re_{\tau 0} = 100$; (b-2) enlarged view of the rectangular region I in (b-1); (c-1) $II^* \leqslant -5040$ for $Re_{\tau 0} = 600$; (c-2) enlarged view of the rectangular region I in (c-1); (d) schematic representation of the vortex structures in the wake region.

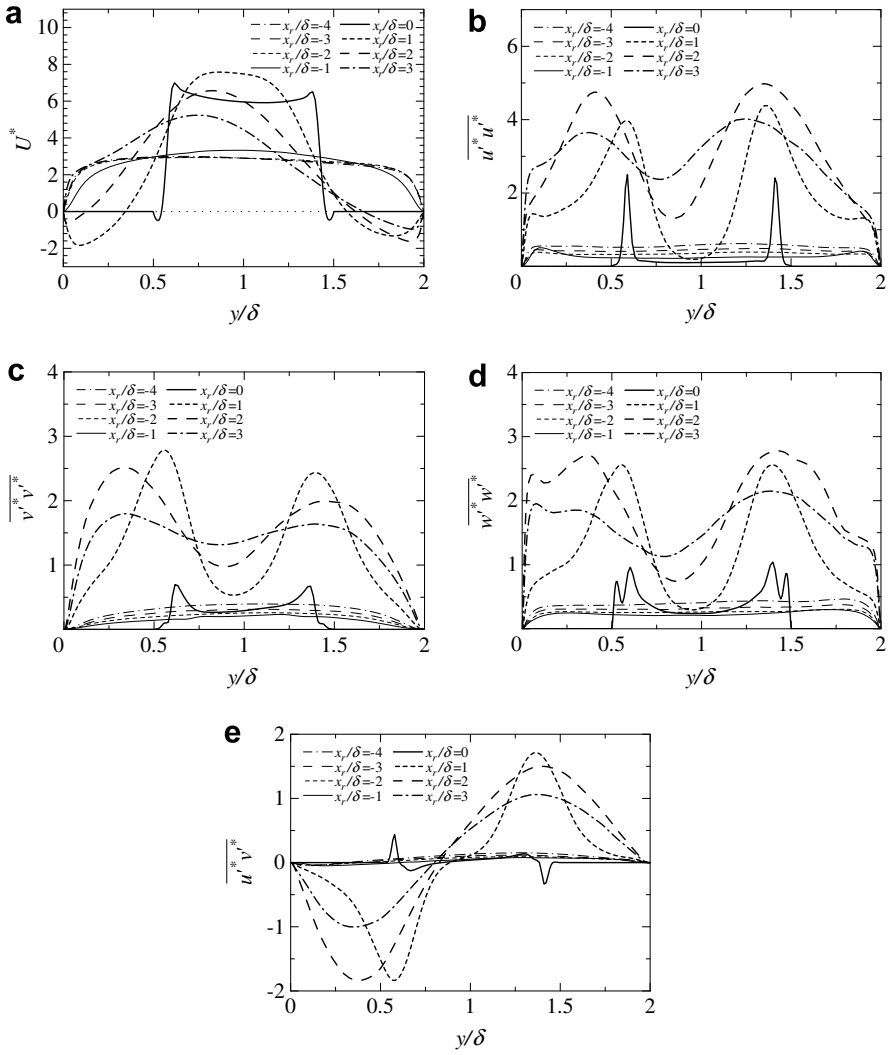

Fig. 7. Profiles of turbulent statistics for $Re_{\tau 0} = 600$. (a) Streamwise mean velocity U^+. (b) Reynolds stress $\overline{u'u'}$; (c) $\overline{v'v'}$; (d) $\overline{w'w'}$; (e) $\overline{u'v'}$.

Molecular diffusion term:

$$D_{ij} = \frac{\partial^2}{\partial x_k^{+2}} \overline{u_i'^* u_j'^*}, \tag{8}$$

Pressure diffusion term:

$$\Pi_{ij} = -\left(\frac{\partial}{\partial x_i^+} \overline{u_j'^* p'^*} + \frac{\partial}{\partial x_j^+} \overline{u_i'^* p'^*} \right), \tag{9}$$

Pressure strain term:

$$\phi_{ij} = \overline{p'^* \frac{\partial u_j'^*}{\partial x_i^+}} + \overline{p'^* \frac{\partial u_i'^*}{\partial x_j^+}}, \tag{10}$$

Dissipation term:

$$\epsilon_{ij} = -2\overline{\left(\frac{\partial u_i'^*}{\partial x_k^+} \right) \left(\frac{\partial u_j'^*}{\partial x_k^+} \right)}, \tag{11}$$

Convection term:

$$C_{ij} = -U_k^* \frac{\partial \overline{u_i'^* u_j'^*}}{\partial x_k^+}, \tag{12}$$

where non-dimensionalized value x_i^+ is $x_i/(\nu/u_{\tau 0})$ with x_1^+, x_2^+ and $x_3^+ = x^+$, y^+ and z^+.

The region ① is the channel center near the slit. The Reynolds stresses and the turbulent energy in this region are much smaller than in other regions as seen in Fig. 7b–d, for instance, the minimum value of the $\overline{u'u'}$ near the channel center is about 4.3 of the maximum value in the shear layer at $x_r/\delta = 1.0$. Fig. 9a and b show the streamwise evolutions of the streamwise mean velocity and the Reynolds stresses, respectively, where U^+ is the non-dimensionalized streamwise mean velocity at the channel center and $\overline{u_i'u_i'}$ indicates the Reynolds stresses on the centerline. The mean velocity increases in the streamwise direction in the range of $5.0 < x/\delta < 7.5$ by the flow acceleration through the slit. In the same region, the values of Reynolds stresses are small; especially, the $\overline{u'u'}$ decreases behind the slit ($6.4 < x/\delta < 7.5$). Fig. 9c shows the

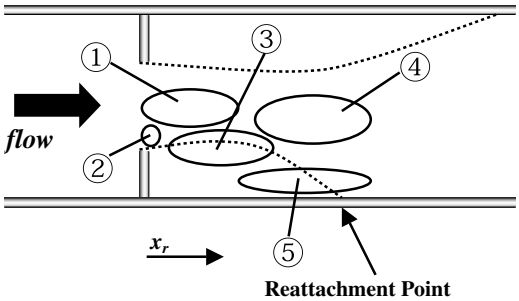

Fig. 8. Classification of the wake region.

vortices behind the slit. No evident vortices are observed in this region. Consequently, the flow is close to the potential flow. This potential region is generated by the flow acceleration.

The region ② occupies the shear layer just behind the slit. Fig. 10a shows the budgets of Reynolds stress $\overline{u'u'}$ in the range of $0.5 < y/\delta < 0.7$ at $x_r/\delta = 0$. The production term balances with the convection one in the shear layers and the negative production can be observed above the shear layers ($y/\delta > 0.6$). The production term of $\overline{u'u'}$ is expressed concretely as

$$P_{11} = -2\overline{u'u'}\frac{\partial U}{\partial x} - 2\overline{u'v'}\frac{\partial U}{\partial y}. \tag{13}$$

In this region ($y/\delta > 0.6$), Reynolds stress $\overline{u'u'}$ exhibits the significant value and the mean velocity gradient $\partial U/\partial x$ is positive as shown in

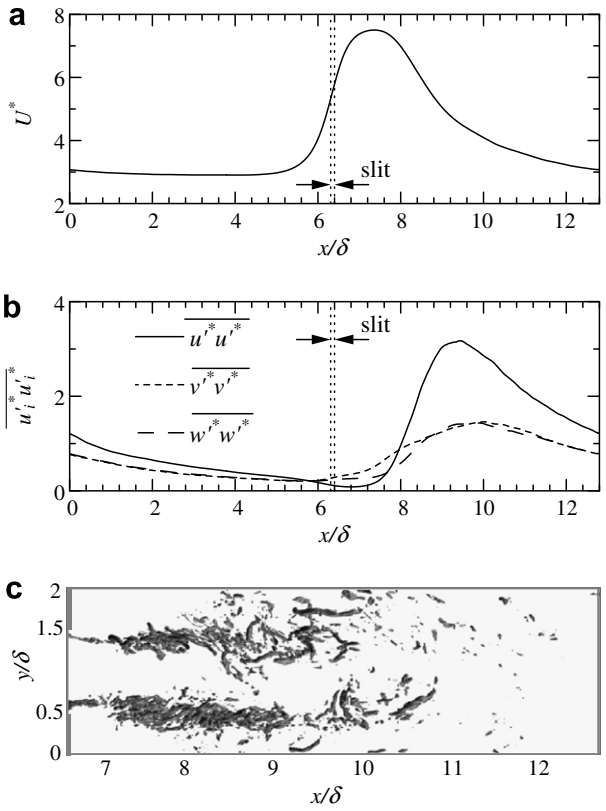

Fig. 9. (a) Streamwise evolution of the streamwise mean velocity on $y/\delta = 1$ line; (b) streamwise evolution of the Reynolds stresses on $y/\delta = 1$ line; (c) vortices behind the slit at $0 < z/\delta < 0.8$ for $Re_{\tau 0} = 600$ ($II^* \leqslant -5000$).

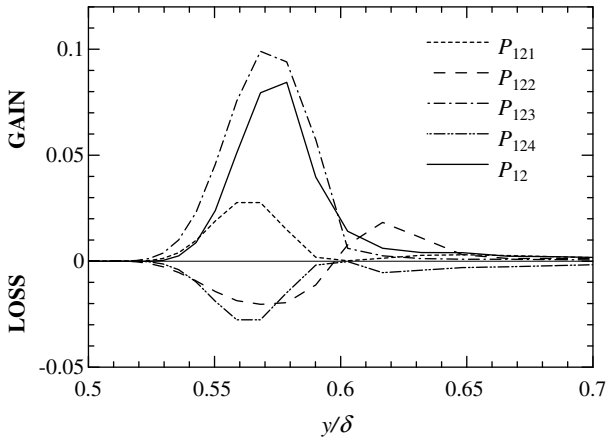

Fig. 11. Terms in the production of $\overline{u'v'}$ in the range of $0.5 < y/\delta < 0.7$ at $x_r/\delta = 0$ for $Re_{\tau 0} = 600$.

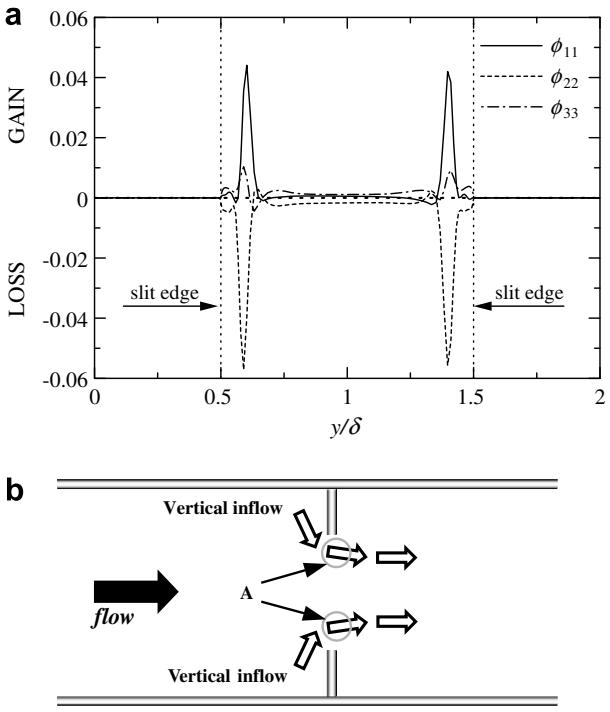

Fig. 12. (a) Profiles of the pressure strain term at $x_r/\delta = 0$ for $Re_{\tau 0} = 600$. (b) Schematic of the inflow through the slit.

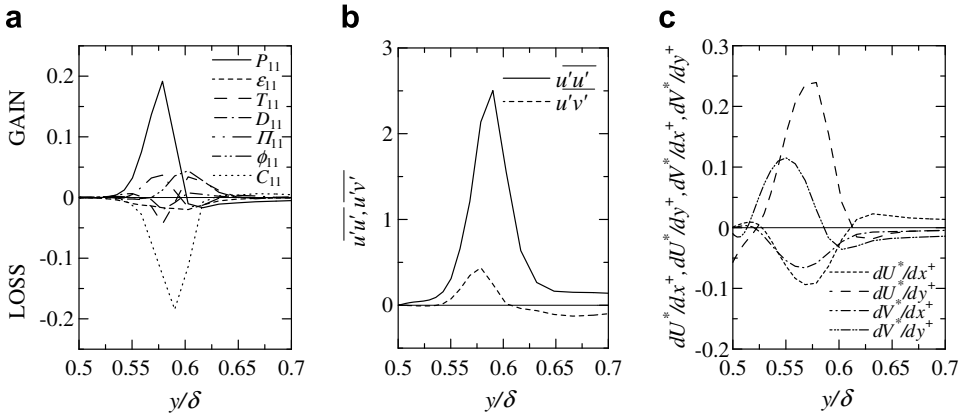

Fig. 10. Profiles in the range of $0.5 < y/\delta < 0.7$ at $x_r/\delta = 0$ for $Re_{\tau 0} = 600$. (a) Terms in the budgets of $\overline{u'u'}$. (b) Reynolds stresses $\overline{u'u'}$ and $\overline{u'v'}$; (c) mean velocity gradients.

Fig. 10b and c. This positive $\partial U/\partial x$ is caused by the flow acceleration through the slit. On the second term of the right-hand side in Eq. (13), the Reynolds shear stress $\overline{u'v'}$ and $\partial U/\partial y$ are negative for $y/\delta > 0.6$ as seen in Fig. 10b and c. The negative mean velocity gradient $\partial U/\partial y$ is caused by the flow contraction (see the former section and Fig. 7a). Therefore, the negative production of $\overline{u'u'}$ is due to the flow acceleration/contraction through the slit.

It is interesting to note that the positive Reynolds shear stress $\overline{u'v'}$ is observed in the shear layer in the lower side of the channel and the negative one in the upper side (see Fig. 7e). In the backward-facing step, $\overline{u'v'}$ never becomes positive. On the other hand, the results of turbulent simulation with the ribs show the negative $-\overline{u'v'}$ (i.e., the positive $\overline{u'v'}$) in the similar region (Ashrafian et al., 2004). The production of $\overline{u'v'}$ becomes positive in the same region as shown in Fig. 11. The concrete expression for production term of $\overline{u'v'}$ is

$$P_{12} = P_{121} + P_{122} + P_{123} + P_{124} = -\overline{u'v'}\frac{\partial U}{\partial x} - \overline{v'v'}\frac{\partial U}{\partial y} - \overline{u'u'}\frac{\partial V}{\partial x} - \overline{u'v'}\frac{\partial V}{\partial y}. \quad (14)$$

Fig. 11 also shows individual terms of the right-hand side in Eq. (13). The third term, i.e., $-\overline{u'u'}\cdot\partial V/\partial x$, is dominant and positive over all the other terms in this region. This sign is caused by the negative mean velocity gradient $\partial V/\partial x$. The wall-normal velocity streamwisely decreases owing to the flow contraction, accordingly the $\partial V/\partial x$ becomes negative through the slit. Thus, the Reynolds shear stress $\overline{u'v'}$ becomes positive by the effect of the flow contraction just behind the slit.

Fig. 12a shows the profiles of the pressure strain term in this region. The redistribution from $\overline{v'v'}$ to $\overline{u'u'}$ is remarkable, i.e., $\phi_{11} > 0$ and $\phi_{22} < 0$. In the opening of the slit, the direction of the flow is changed due to the flow contraction (see region A in Fig. 12b). The transport process of the turbulent energy in the vertical direction is impeded and the one in the streamwise direction is promoted in this region. This is similar to the so-called splatting effect observed near the wall of the channel flow although there is no solid wall in this region. Therefore, the redistribution process from $\overline{v'v'}$ to $\overline{u'u'}$ is enhanced through the slit.

The region ③ indicates the shear layer in the recirculation region. Fig. 13a shows the terms in the budget of $\overline{u'u'}$ at $x_r/\delta = 0.5$. These profiles are characterized by the sharp peaks of the production and the large negative pressure strain for $0.5 < y/\delta < 0.75$ on the lower side. The peak production is caused by the large positive mean velocity gradient $\partial U/\partial y$. In the budgets of $\overline{u'v'}$, the $\partial U/\partial y$ also mainly contributes to the negative peak of the production term (not shown here). Fig. 11b and c display the budget terms of $\overline{v'v'}$

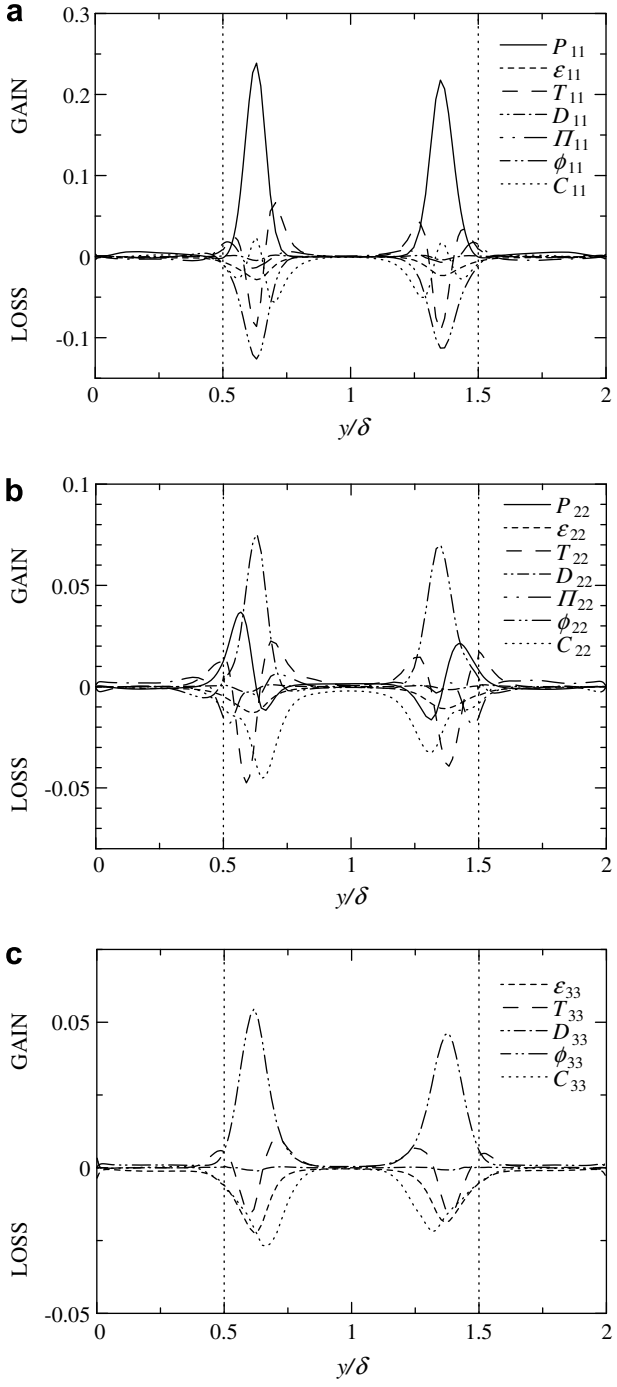

Fig. 13. Terms in the budgets of Reynolds stresses at $x_r/\delta = 0.5$ for $Re_{\tau 0} = 600$. (a) $\overline{u'u'}$; (b) $\overline{v'v'}$; (c) $\overline{w'w'}$.

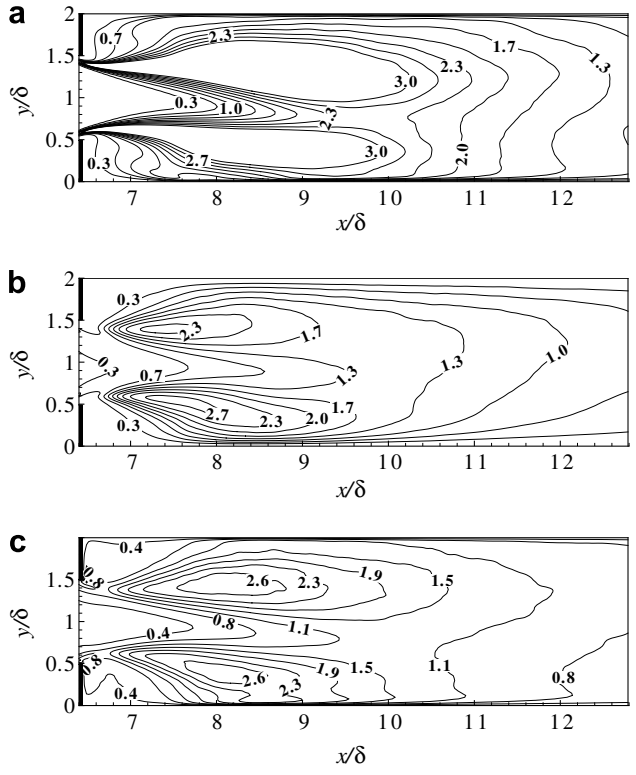

Fig. 14. Reynolds stress distributions behind the slit. (a) $\overline{u'u'}$; (b) $\overline{v'v'}$; (c) $\overline{w'w'}$.

and $\overline{w'w'}$ at $x_r/\delta = 0.5$. In the shear layer, the pressure strain terms of $\overline{v'v'}$ and $\overline{w'w'}$ exhibit large positive values. Hence, the redistribution from $\overline{u'u'}$ to $\overline{v'v'}$ and $\overline{w'w'}$ is the dominant process in this region.

The maps of $\overline{u'u'}$, $\overline{v'v'}$ and $\overline{w'w'}$ are shown in Fig. 14. In the shear layer near the slit ($6.4 < x/\delta < 6.8$), only $\overline{u'u'}$ exhibits large value, which corresponds to the region of the large positive production by mean velocity gradient $\partial U/\partial y$ noted above. No large values are seen in $\overline{v'v'}$ and $\overline{w'w'}$ in the same region. In the range for $x/\delta > 6.8$, on the other hand, they exhibit large values as $\overline{u'u'}$ does. These profiles are equivalent for the redistribution from $\overline{u'u'}$ to $\overline{v'v'}$ and $\overline{w'w'}$ discussed above. It is worth noting that the budgets of the Reynolds stresses and the turbulent kinetic energy in this region are similar to those of a backward-facing step flow (Le et al., 1997) and a plane mixing layer (Rogers and Moser, 1993). In addition, on the turbulent structures in this region, the K–H vortices caused by the streamwise instability are distorted and break up into three-dimensional structures discussed in the former section. This scenario also corresponds to the redistribution process in this shear layer.

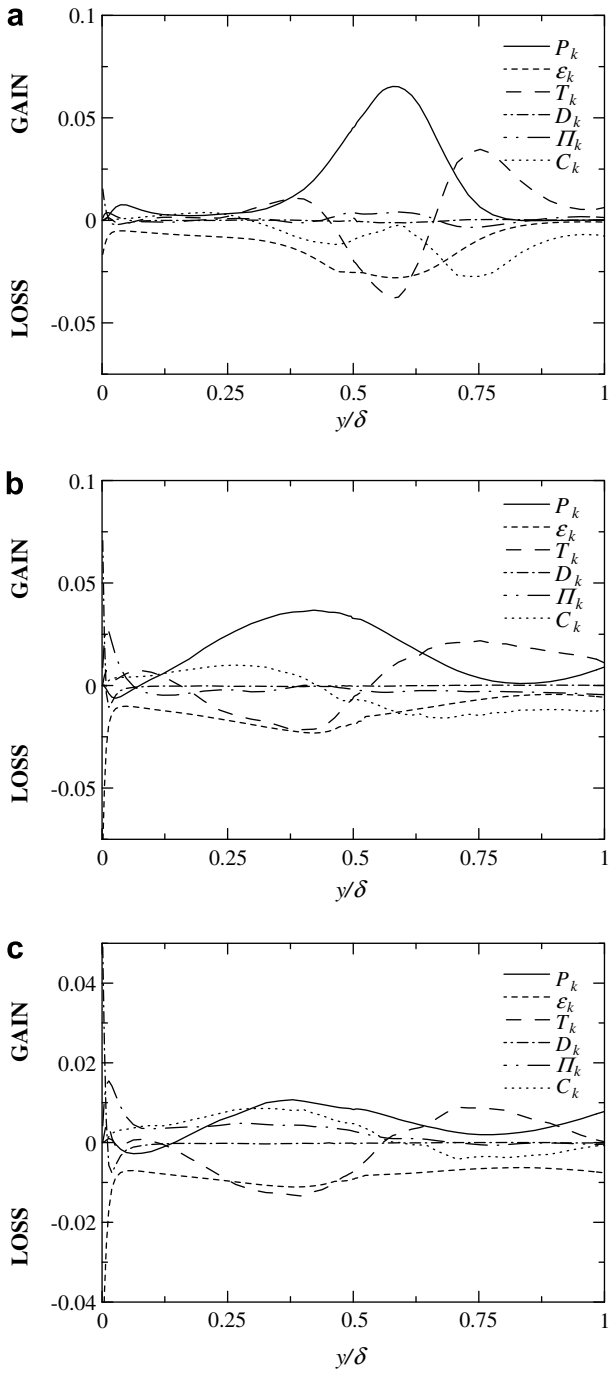

Fig. 15. Terms in the budgets of turbulent kinetic energy on the lower side of the channel for $Re_{\tau 0} = 600$. (a) $x_r/\delta = 1$; (b) $x_r/\delta = 2$; (c) $x_r/\delta = 3$.

In the region ④ ($x/\delta > 8$ and $0.5 < y/\delta < 1$ on the lower side of the channel), the turbulent diffusion term plays an important role as shown in Fig. 15a–c. This term removes the turbulent energy from the shear layers and transports it to the channel center. The contribution of the turbulent diffusion to the budgets becomes larger downstream in the center region of the flow (the center of the channel, i.e., $y/\delta = 1.0$, is not equal to the flow center because of the flow asymmetry). Thus, the turbulent diffusion contributes to the increase of the Reynolds stresses and the turbulent kinetic energy in the central region. The vortices are also generated in the same region as shown in Fig. 9c. On the other hand, Le et al. (1997) has reported that the turbulent diffusion term transfers the turbulent energy to the near wall region in their simulation of a backward-facing step. In the present study, two symmetric shear layers are generated closely with each other. Therefore, the turbulent diffusion adds more effects on the turbulent statistics at the channel center than in the case of the backward-facing step flow.

The region ⑤ is located near the reattachment point (cf. the time-averaged reattachment length $L_{r1}/\delta \simeq 2.6$ on the lower side for $Re_{\tau 0} = 600$). Fig. 16 displays the profiles of the pressure strain term at $x_r/\delta = 0.5$, 2 and 3.5. Near the region (5 in circle), the pressure 70% of the ϕ_{33} as shown in Fig. 16b. This is much larger than in other regions (Fig. 16a and c) or in turbulent plane channel flows because of the large scale splatting effect due to the flow reattachment.

4. Conclusion

In the present study, we performed DNS of turbulent channel flow with the periodic two-dimensional slits in various Reynolds numbers for $10 < Re_{\tau 0} < 1500$ ($40 < Re_b < 7800$) and investigated the asymmetry phenomena, mean reattachment length, vortex structures and the relationship between turbulence statistics and structures.

The mean flow becomes asymmetric behind the slit because of the Coanda effect. In this study, this asymmetry phenomena can be observed for $30 < Re_{\tau 0} < 7800$, i.e., $180 < Re_b < 7800$. The Reynolds number dependence upon the reattachment length is similar to those described in the case of the backward-facing step experiments (Armaly et al., 1983). The sharp decrease in the reattachment length is observed at $Re_b \simeq 400$. This is the transition from laminar to turbulence. The secondary bubble can be seen in the turbulent regime. The length becomes constant in the higher Reynolds number range.

The large-scale K–H vortices are generated just behind the slit. In the lower Reynolds number, the structure similar to the'helical-pairing structure' in a mixing layer can be observed. This structure becomes more complex with the increase of the Reynolds number. The complex three-dimensional vortex structure with a lattice pattern is generated in the higher Reynolds number regime. This generation – deformation – breaking up scenario resembles that of turbulent mixing layer and backward-facing step turbulence.

The budgets of the turbulent kinetic energy and Reynolds stresses were calculated. We classified the wake region into five regions based upon the budgets of the Reynolds stresses and the turbulent structures. The several differences are found between the Reynolds stresses budgets in the present case and those in a backward-fac-

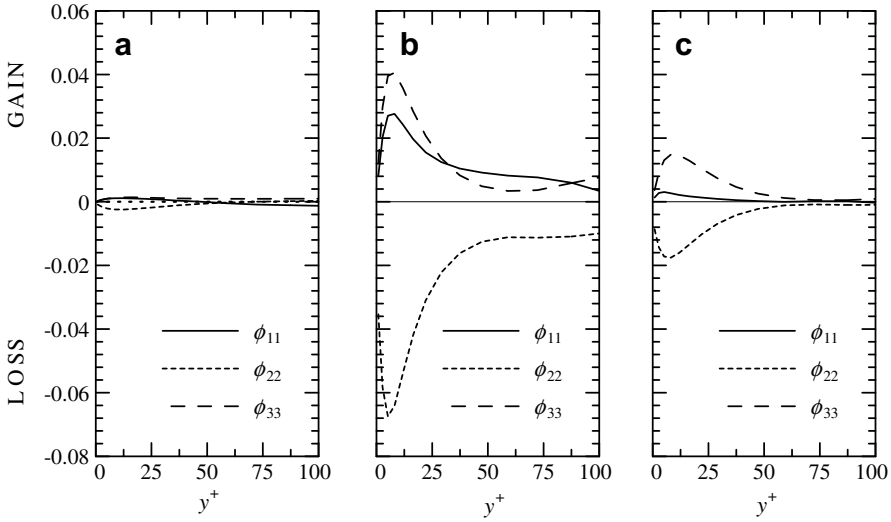

Fig. 16. Pressure strain profiles near the lower wall for $Re_{\tau 0} = 600$. (a) $x_r/\delta = 0.5$; (b) $x_r/\delta = 2$; (c) $x_r/\delta = 3.5$.

ing step turbulence. The potential region is generated in the channel center near the slit. In the shear layers just behind the slit, the Reynolds shear stress $\overline{u'v'}$ becomes positive owing to the effect of the flow contraction. In addition, the production term of $\overline{u'u'}$ exhibits its negative value near the slit edge. This is because of the flow acceleration/contraction effects. These behaviors cannot be observed in the backward-facing step turbulence. At the shear layer in the recirculation region, the redistribution from $\overline{u'u'}$ to $\overline{v'v'}$ and $\overline{w'w'}$ is the dominant process. In the channel center at the recirculation region, the turbulent diffusion term transfers the turbulent energy from the shear layer to the channel center. In the wall vicinity of the recirculation region, the redistribution from $\overline{v'v'}$ to $\overline{u'u'}$ is promoted by the large scale splatting effect.

Acknowledgements

The present study was supported by "Research Center for the Holistic Computational Science (Holcs)" of the Ministry of Education, Culture, Sports, Science and Technology (MEXT). A part of the present computations was performed with use of the supercomputing resources at Information Synergy Center of Tohoku University.

References

Alleborn, N., Nandakumar, K., Raszillier, H., Durst, F., 1997. Further contributions on the two-dimensional flow in a sudden expansion. J. Fluids Mech. 330, 169–188.

Armaly, B.F., Durst, F., Pereira, J.C.F., Schonung, B., 1983. Experimental and theoretical investigation of backward-facing step flow. J. Fluids Mech. 127, 473–496.

Ashrafian, A., Andersson, H.I., Manhart, M., 2004. DNS of turbulent flow in a rod-roughened channel. Int. J. Heat Fluid Flow 25, 373–383.

Avancha, R.V.R., Pletcher, R.H., 2002. Large eddy simulation of the turbulent flow past a backward-facing step with heat transfer and property variations. Int. J. Heat Fluid Flow 23, 601–614.

Chen, Y.T., Nie, J.H., Armaly, B.F., Hsieh, H.T., 2006. Turbulent separated convection flow adjacent to backward-facing step – effects of step height. Int. J. Heat Mass Transfer 49, 3670–3680.

Cherdron, W., Durst, F., Whitelaw, J.H., 1978. Asymmetric flows and instabilities in symmetric ducts with sudden expansion. J. Fluids Mech. 84, 13–31.

Choi, H.S., Suzuki, K., 2005. Large eddy simulation of the turbulent flow and heat transfer in a channel with one wavy wall. Int. J. Heat Fluid Flow 26, 681–694.

Comte, P., Lesieur, M., Lamballais, E., 1992. Large- and small-scale stirring of vorticity and a passive scalar in a 3-D temporal mixing layer. Phys. Fluids 12, 2761–2778.

Durst, F., Pereira, J.C.F., Tropea, C., 1993. The plane symmetric sudden-expansion flow at low Reynolds numbers. J. Fluids Mech. 248, 567–581.

Fadlum, E.A., Verzicco, R., Orlandi, P., Mohd-Yusof, J., 2000. Combined immersed-boundary finite-difference methods for three-dimensional complex flow simulations. J. Comput. Phys. 161, 35–60.

Fearn, R.M., Mullin, T., Cliffe, K.A., 1990. Nonlinear flow phenomena in a symmetric sudden expansion. J. Fluids Mech. 211, 595–608.

Friedrich, R., Arnal, M., 1990. Analysing turbulent backward-facing step flow with the lowpass-filtered Navier–Stokes equations. J. Wind Eng. Ind. Aerodyn. 35, 101–128.

Inagaki, M., Kondoh, T., Nagano, Y., 2005. A mixed-time-scale SGS model with fixed model-parameters for practical LES. J. Fluids Eng. 127, 1–13.

Kawamura, H., Abe, H., Matsuo, Y., 1999. DNS of turbulent heat transfer in channel flow with respect to Reynolds and Prandtl number effects. Int. J. Heat Fluid Flow 20, 196–207.

Krogstad, P.-A., Andersson, H.I., Bakken, O.M., Ashrafian, A., 2005. An experimental and numerical study of channel flow with rough walls. J. Fluids Mech. 530, 327–352.

Le, H., Moin, P., Kim, J., 1997. Direct numerical simulation of turbulent flow over a backward-facing step. J. Fluids Mech. 330, 349–374.

Leonardi, S., Orlandi, P., Smalley, R.J., Djenidi, L., Antonia, R.A., 2003. Direct numerical simulation of turbulent channel flow with transverse square bars on one wall. J. Fluids Mech. 491, 229–238.

Lesieur, M., 1997. Turbulence in Fluids. Kluwer Academic Publishers. p. 438.

Nagano, Y., Hattori, H., Houra, T., 2004. DNS of velocity and thermal fields in turbulent channel flow with transverse-rib roughness. Int. J. Heat Fluid Flow 25, 393–403.

Neto, A.S., Grand, D., Metais, O., Lesieur, M., 1993. A numerical investigation of the coherent vortices in turbulence behind a backward-facing step. J. Fluids Mech. 256, 1–25.

Rogers, M.M., Moser, R.D., 1993. Direct simulation of a self-similar turbulent mixing layer. Phys. Fluids 6, 903–923.

Sewall, E.A., Tafti, D.K., Graham, A.B., Thole, K.A., 2006. Experimental validation of large eddy simulations of flow and heat transfer in a stationary ribbed duct. Int. J. Heat Fluid Flow 27, 243–258.

Stalio, E., Nobile, E., 2003. Direct numerical simulation of heat transfer over riblets. Int. J. Heat Fluid Flow 24, 356–371.